Experimental determination of the ^{26}Al$(n, \alpha)^{23}$Na reaction cross section and calculation of the Maxwellian averaged cross section at stellar temperatures

L. De Smet* and C. Wagemans†
Department of Subatomic and Radiation Physics, University of Gent, Proeftuinstraat 86, B-9000 Gent, Belgium

J. Wagemans
SCK•CEN, Boeretang 200, B-2400 Mol, Belgium

J. Heyse‡ and J. Van Gils
Institute for Reference Materials and Measurements, EC-JRC, Retieseweg 111, B-2440 Geel, Belgium
(Received 19 February 2007; revised manuscript received 15 May 2007; published 25 October 2007)

The ^{26}Al$(n, \alpha)^{23}$Na reaction cross section has been studied at the linear accelerator GELINA of the Institute for Reference Materials and Measurements in Geel, Belgium, and has been determined up to a neutron energy of about 100 keV using the time-of-flight technique. Six resonances could be observed in this energy region, whereas before only one had been identified experimentally. For four of them, resonance parameters such as resonance energy, total width, area, and spin of the state could be determined. From the obtained ^{26}Al$(n, \alpha)^{23}$Na cross section data, Maxwellian averaged cross section (MACS) values were calculated by numerical integration. Since neutron induced reactions are among the major destruction mechanisms of ^{26}Al in our Galaxy, these new MACS values contribute to a better understanding of the observed ^{26}Al abundance.

DOI: 10.1103/PhysRevC.76.045804 PACS number(s): 25.40.Fq, 21.10.Hw, 27.30.+t, 97.10.Cv

I. INTRODUCTION

The origin and destruction of radioactive ^{26}Al in our Galaxy has gained a lot of interest in the last few decades. ^{26}Al decays to the first excited state of ^{26}Mg, which deexcites to the ground state by emitting a 1.809 MeV γ ray. These γ rays were detected for the first time by the HEAO-3 satellite [1] and confirmed by many subsequent observations. The COMPTEL imaging telescope aboard NASA's Compton γ ray observatory provided the first-ever image of the sky in emission from radioactive ^{26}Al [2]. Since the half-life of ^{26}Al, $T_{\frac{1}{2}} = 7.17 \times 10^5$ yr, is much shorter than the time scale for galactic evolution—the age of our Galaxy is of the order of 10^{10} years—this map reveals information on recent and ongoing nucleosynthesis in large and extended parts of our Galaxy.

Secondly, ^{26}Mg overabundances were found in meteoritic material, indicating that ^{26}Al was present at the formation of the meteoroid. Its decay produced the ^{26}Mg excess. As meteoroids arose when the Solar System formed some 4.6×10^9 yr ago, such isotopic anomalies found in meteorites can provide information on the birth of the Solar System and on stellar nucleosynthesis.

The origin of the observed ^{26}Al is still an open question. To be observable in γ ray spectra and to be present in meteorites in the form of ^{26}Mg excess, ^{26}Al has to be ejected in the interstellar medium before destruction. This can be achieved in explosive sites (supernovae) or in stars suffering extensive mass loss through stellar winds such as asymptotic giant branch (AGB) stars [3–7] or Wolf-Rayet (WR) stars [8]. Recently, Wasserburg *et al.* [3] concluded that supernova explosions are not acceptable scenarios for providing the observed ^{26}Al, while it could be produced in AGB stars. The aluminum isotopes are then produced in three sites [9]: in the H-burning shell via the Mg-Al chain [10], in the He-burning shell via α capture on ^{22}Ne, and at the base of the convective envelope in the most massive AGB stars that experience hot bottom burning (HBB) via the Mg-Al chain. Following the models used in Ref. [9], HBB, which occurs only in massive AGB stars, is the most effective site of the three mentioned above for the production of ^{26}Al. However, during the interpulse phase of the third dredge up in AGB stars, a rich nucleosynthesis occurs through the release of neutrons via the ^{13}C$(\alpha, n)^{16}$O reaction. When in these three sites the temperature becomes high enough, the ^{26}Al(n, α) and ^{26}Al(n, p) chains may open and destroy the formed ^{26}Al.

As discussed above and in more detail by Koehler *et al.* [11], neutron induced reactions on ^{26}Al have an influence on its final abundance. Unfortunately, very few experimental data are available: the only neutron induced measurements on ^{26}Al above thermal energy are the ^{26}Al$(n, p)^{26}$Mg measurement by Trautvetter *et al.* [12] and the ^{26}Al$(n, p_1)^{26}$Mg and ^{26}Al$(n, \alpha_0)^{23}$Na measurements performed by Koehler *et al.* [11]. Trautvetter *et al.* [12] determined the partial cross section and corresponding reaction rate for four neutron energies. The measurements of Koehler *et al.* [11] resulted in a cross section determination from thermal energy up to 70 keV for the (n, p_1) reaction and up to 10 keV for the (n, α_0) reaction; in the (n, α_0) reaction, they only observed one resonance.

*liesbeth.desmet@gmail.com
†cyrillus.wagemans@UGent.be
‡Present address: SCK•CEN, Boeretang 200, B-2400 Mol, Belgium.

The present work extends the energy range, leading to the observation of more resonances, which were predicted through inverse reactions by Skelton *et al.* [13]. Moreover, interesting nuclear physics information could be derived from the cross section data such as total level width, strength, and spin of the states in the compound nucleus. Partial or preliminary results have already been reported [14,15]. For a detailed description of the experimental setup, data reduction, and results, the reader is referred to Ref. [16].

From the ^{26}Al$(n,\alpha)^{23}$Na cross section data obtained in this work, Maxwellian averaged cross section (MACS) values were calculated. These values replace the theoretical values in the stellar network calculations over the measured energy range.

II. EXPERIMENTAL SETUP AND DATA REDUCTION

A. Experimental setup

The ^{26}Al$(n,\alpha)^{23}$Na reaction was studied at an 8.45 m flight path of the GELINA linear accelerator time-of-flight facility at the Institute for Reference Materials (IRMM) in Geel, Belgium. The linac produces a pulsed electron beam. The high-energy electrons hit a cooled and rotating uranium target, in which they are slowed down and generate Bremsstrahlung γ rays. Neutrons are then produced via (γ, n) and (γ, f) reactions in the uranium target itself. To increase the number of slow neutrons, two water-filled beryllium moderators are placed above and below the uranium target. The resulting neutron energy distribution can be characterized by a Maxwellian distribution at thermal energy and a high energy tail with approximately a $1/E$ energy dependence. The neutron energy spectrum ranges from a few meV up to a few MeV. The time-of-flight (TOF) method is applied to determine the energy of the interacting neutrons. Detailed information about the GELINA facility can be found in Refs. [17,18].

The accelerator was operated at a repetition frequency of 800 Hz, and the electron bursts had a width of 1 ns. To remove neutrons from previous bursts, a Cd overlap filter was permanently used in the neutron beam. The TOF-dependent background was determined in a separate measurement by putting black resonance filters such as Au, Co, Mn, Rh, and W in the neutron beam.

For the detection of the α particles, a Frisch gridded ionization chamber filled with ultrapure methane as detector gas was used, leading to a 2π detection geometry. The chamber is shown in Fig. 1. The entrance windows were made of Mylar instead of the generally used natural Al (^{27}Al) material, because ^{27}Al has a neutron resonance at 5.9 keV, which unfortunately is also the energy of a strong resonance in ^{26}Al(n,α_0) [11,14].

From the level scheme in Fig. 2, it is clear that both (n, p) and (n,α) reactions are possible. Table I gives the Q values and corresponding energies of the protons and α particles produced in the ^{26}Al(n,α_i) and ^{26}Al(n, p_i) reactions. The gas pressure and electrode distances of the ionization chamber were chosen in such a way that the α particles lose their energy completely in the detection volume, while the protons only lose part of their energy (less than the energy of the α_1 particles). The electric field was then matched to the chosen pressure and electrode distances to have the best possible signal formation.

TABLE I. Q values and corresponding ejectile energies for the possible ^{26}Al$(n,\alpha_i)^{23}$Na and ^{26}Al$(n, p_i)^{26}$Mg reactions.

	Q value (MeV)	E (MeV)
p_0	4.78	4.60
p_1	2.98	2.87
p_2	1.85	1.78
α_0	2.97	2.53
α_1	2.53	2.16
α_2	0.89	0.76

The signals from the anode and cathode were amplified and sent to an analog-to-digital converter (ADC). A third signal was sent from the amplifier on the cathode side to a timing single channel analyzer (TSCA). If this signal lies between some predefined levels, a fast logic signal T_n is sent to a time coder (TC) and serves as a stop signal. The start signal T_0 is generated by the linear accelerator and is sent to the time coder just before the electrons impinge on the uranium target. The TC measures the time difference between T_n and T_0 for each event and converts it into a TOF channel number. At this point, both ADC and TOF channel numbers are handled by the LABVIEW-based data acquisition system 2000-DAQ developed at the IRMM [19] and are stored on a personal computer (PC) for off-line analysis.

The preparation of the ^{26}Al sample was done in two steps. First, ^{26}Al was produced at the Los Alamos National Laboratory (USA) by spallation of a KCl target with a proton beam and purified by ion exchange. This resulted in a batch of material with a ^{26}Al/^{27}Al ratio of 0.1. To deposit as much as possible of the produced ^{26}Al, electrodeposition of the Al dissolved in a HCl solution was used in a second step at the IRMM. This method has already been applied successfully at

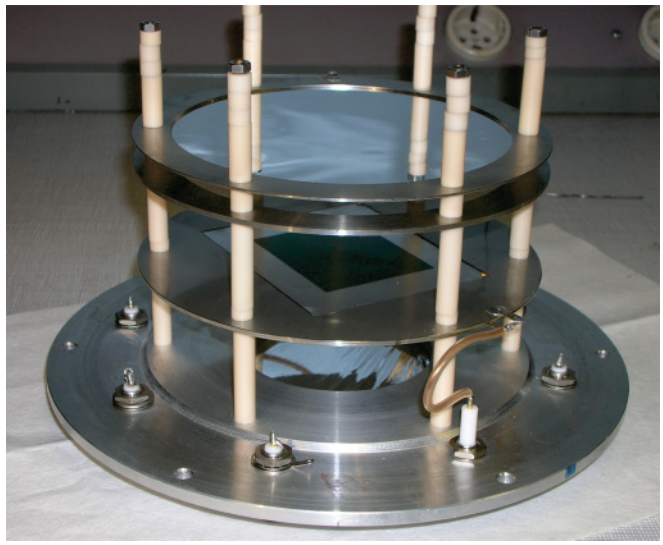

FIG. 1. (Color online) Frisch gridded ionization chamber used in this work. The sample is mounted in the middle of the cathode, which is the lowest plate in the picture. The top plate is the anode; the plate in the middle is the Frisch grid.

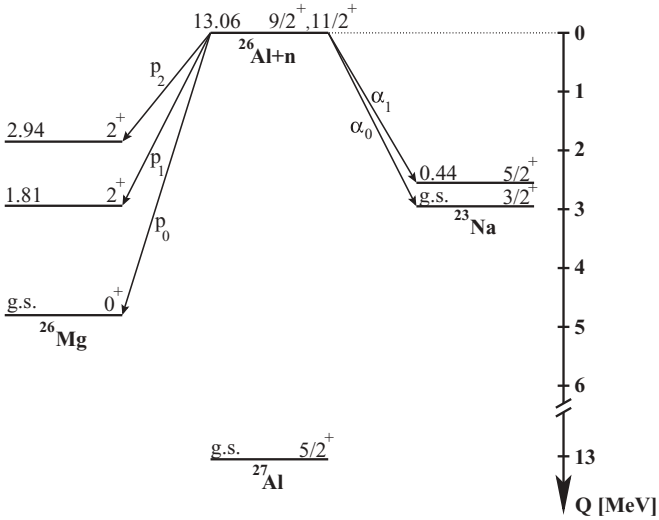

FIG. 2. Level scheme for the ^{26}Al$(n, \alpha_i)^{23}$Na and ^{26}Al$(n, p_i)^{26}$Mg reactions. The energies are given in MeV.

the IRMM for the preparation of several other samples [20,21]. The method relies on the migration of positive or negative species to a substrate of appropriate polarity and precipitation as a compound. To check whether this method could be used for ^{26}Al as well, several tests were first performed with a natural aluminum solution. Because a deposition of ^{27}Al on an aluminum backing cannot be distinguished, a nickel foil was chosen as the backing material. The effective area of the ^{26}Al sample was 6×5 cm^2. The mass determination was done with a calibrated germanium detector, which detected the 1.809 MeV γ rays originating from the deexcitation of ^{26}Mg to its ground state. This ^{26}Mg is formed in the β decay of ^{26}Al. This resulted in a ^{26}Al sample containing $(2.58 \pm 0.12) \times 10^{17}$ ^{26}Al atoms. A detailed description of the preparation and characterization of the ^{26}Al target can be found in Refs. [22,23].

For the neutron flux determination, an evaporated elemental ^{10}B layer was used, containing $(1.14 \pm 0.01) \times 10^{20}$ ^{10}B atoms, on a 6×5 cm^2 effective area. This number was determined in a dedicated measurement relative to the ^{235}U(n, f) reference cross section (see Ref. [16] for details).

B. Data reduction

The differential neutron induced cross section of ^{26}Al can be calculated as [24]

$$\sigma_{^{26}\mathrm{Al}}(E_n) = \frac{\epsilon_{^{10}\mathrm{B}}}{\epsilon_{^{26}\mathrm{Al}}} \frac{Y_{^{26}\mathrm{Al}}(E_n) - Y^{\mathrm{BG}}_{^{26}\mathrm{Al}}(E_n)}{Y_{^{10}\mathrm{B}}(E_n) - Y^{\mathrm{BG}}_{^{10}\mathrm{B}}(E_n)} \frac{N_{^{10}\mathrm{B}}}{N_{^{26}\mathrm{Al}}} \sigma_{^{10}\mathrm{B}}(E_n), \quad (1)$$

with Y_i the total observed count rate, N_i the number of atoms in the samples used, ϵ_i the detector efficiency, and $\sigma_{^{10}\mathrm{B}}$ the known ^{10}B$(n, \alpha)^7$Li cross section which was taken from the ENDF/B-VI database [25]. The time-dependent background Y_i^{BG}(TOF), which is equivalent to the energy-dependent background $Y_i^{\mathrm{BG}}(E_n)$, has been determined by fitting a function $Y^{\mathrm{BG}}(\mathrm{TOF}) = a\mathrm{TOF}^b + c$ through the count rates in the black resonance regions. The result for the ^{10}B$(n, \alpha)^7$Li reaction is shown in Fig. 3. Then, the background was subtracted from the count rate Y_i(TOF). Since the ^{26}Al(n, α) and the

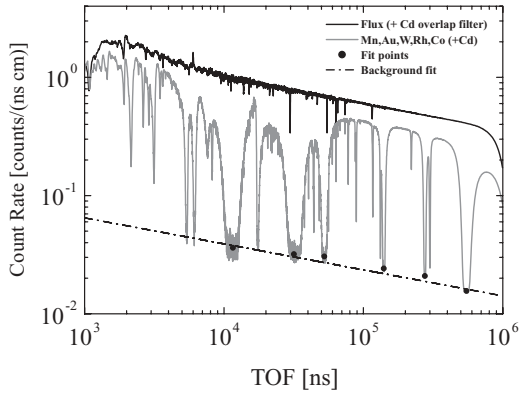

FIG. 3. Background fit through the black resonance regions, represented by the dots, for the ^{10}B$(n, \alpha)^7$Li reaction.

^{10}B(n, α) reactions were determined in the same experimental conditions, $\epsilon_{\mathrm{B}}/\epsilon_{\mathrm{Al}} = 1$.

The pulse height vs the time-of-flight for the ^{26}Al(n, α) measurement is shown in Fig. 4. The black zone around the anode pulse height channel 400, which ranges over the complete TOF channel region, represents ^{10}B(n, α) counts caused by the presence of a non-negligible amount of ^{10}B in the ^{26}Al sample. The arrows show the positions of the ^{26}Al(n, α_i) resonances. The ^{26}Al(n, α_i) reactions can be selected by putting appropriate software windows on the anode and cathode pulse height spectra. Figure 4 shows that it is even possible to separate the α_0 particles from the α_1 particles (which are, respectively, above and below the anode pulse height channel number 640). As a result, it is concluded that the first resonance at the highest TOF ($\sim$ channel 850) is mainly α_0, with $\alpha_0/(\alpha_0 + \alpha_1) = 0.87 \pm 0.03$; the second one (TOF $\sim$ channel 380) is only α_0; the third one (TOF $\sim$ channel 280) is only α_1; and finally the fourth resonance (TOF $\sim$ channel 250) is a mixture of α_0 and α_1, with $\alpha_0/(\alpha_0 + \alpha_1) = 0.55 \pm 0.05$. Below TOF channel number 250 (corresponding to neutron energies above 45 keV), two resonances can be observed. However, these two resonances are too close to the γ flash. This strong γ flash is caused by the slowing down of the electrons in the U target, resulting in a distortion in the electronic measuring chain. Therefore, one can only determine the energy position of these two resonances, but a resonance analysis is not possible. For the same reason, the cross section data above 45 keV neutron energy are considered to be less reliable.

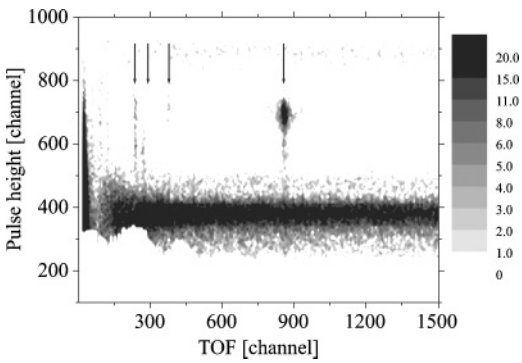

FIG. 4. Anode vs TOF spectrum for the ^{26}Al(n, α_i) measurement.

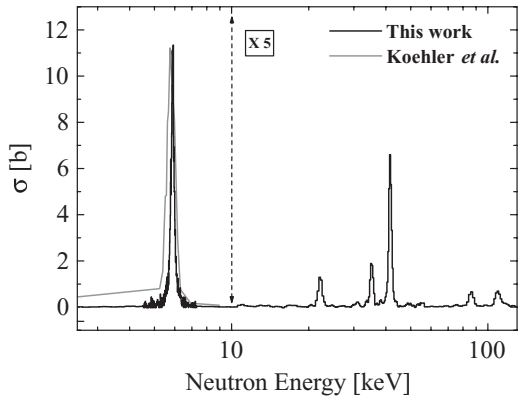

FIG. 5. ^{26}Al$(n, \alpha_0 + \alpha_1)^{23}$Na cross section determined in this work (black line) compared with the ^{26}Al$(n, \alpha_0)^{23}$Na cross section obtained by Koehler *et al*. [11] (gray line).

III. RESULTS

A. Cross section

The data have been analyzed using AGS, a computer code for uncertainty propagation in time-of-flight cross section data which was developed at IRMM [26,27]. The code performs a full propagation of uncertainties, starting from the uncorrelated uncertainties due to counting statistics. The final output includes a complete covariance matrix accounting for both correlated and uncorrelated uncertainty components. The sources of uncertainties can be divided into three categories: statistical, overall normalization, and neutron-energy-dependent systematic uncertainties. For a given measuring time and neutron flux, the statistical uncertainties depend on the cross sections of the measured reactions and, as a consequence, strongly vary with neutron energy. The overall normalization uncertainty of the data is determined by the uncertainties in the number of atoms in the ^{26}Al and ^{10}B samples used and by the uncertainty in the ^{10}B(n, α) reference cross section. Finally, there is the uncertainty in the correction for the time-dependent background.

The obtained ^{26}Al$(n, \alpha)^{23}$Na cross section is shown in Fig. 5. Six resonances can be observed; however, as mentioned before, at higher energies (>45 keV), one can only conclude that there is a resonance at that energy position, but the resonances cannot be considered in a resonance analysis. The obtained cross section is compared with the results of an experiment performed by Koehler *et al*. at the Los Alamos Neutron Science Center (LANSCE) [11]. They measured the ^{26}Al$(n, p_1)^{26}$Mg and ^{26}Al$(n, \alpha_0)^{23}$Na cross sections from thermal energy up to, respectively, 70 and 10 keV. It is clear that the resonance at 6 keV observed by Koehler *et al*. during the ^{26}Al$(n, \alpha_0)^{23}$Na cross section measurement had a much larger area than the one observed here; however, their measurement had an uncertainty of 26%. This uncertainty was due to the much smaller number of atoms in the ^{26}Al sample used by them (4×10^{15} ^{26}Al atoms), which is almost 65-fold less than the sample used in the present study. Moreover, they used surface barrier detectors in a $\Delta E/E$ telescope setup, thus the detection geometry was much lower than in this work. This made the measurement sensitive to anisotropy effects and the flux determination more difficult [14].

B. Resonance analysis

1. Fitting procedure

As explained in a previous article [24], resonances in experimental cross sections can be fitted with Voigt shapes to take into account the broadening of the resonances due to the experimental resolution Δ_G. A Voigt expression is a convolution of a Gauss and a Breit-Wigner function, where the Gaussian contribution represents the experimental broadening

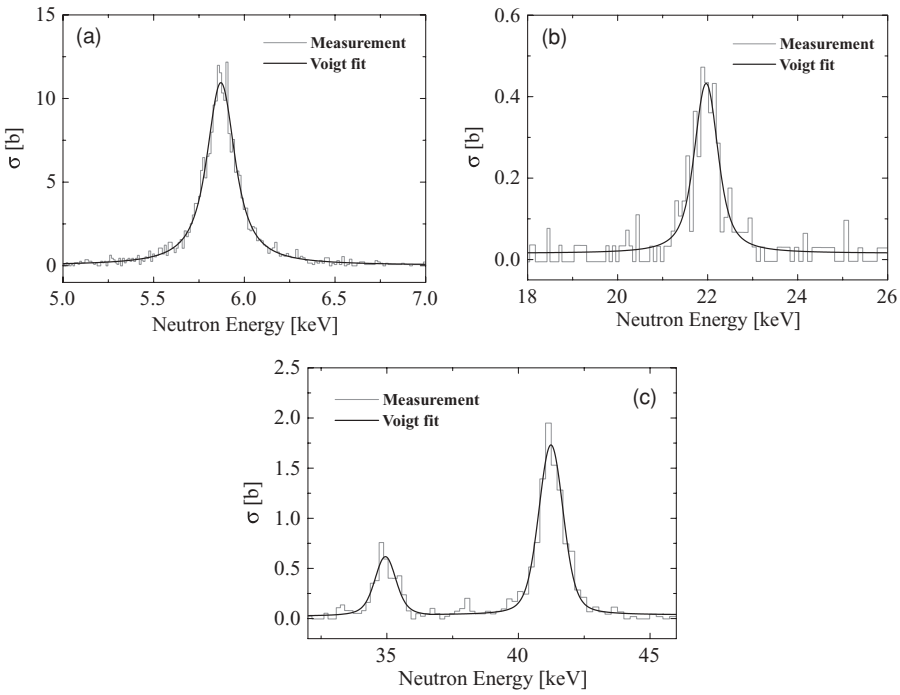

FIG. 6. Voigt fits to the ^{26}Al$(n, \alpha_0 + \alpha_1)^{23}$Na cross section data for the four resonances.

TABLE II. Resonance parameters

	Energy (eV)	Area (b eV)	Γ (eV)	ω_α (eV)	ω_{α_0} (eV)	J^π
This work[a]	5870 ± 20	2950 ± 250	160 ± 25	4.23 ± 0.36	3.68 ± 0.34	$[\frac{7}{2}^- - \frac{13}{2}^-]$
	21980 ± 100	340 ± 50	400 ± 100	1.83 ± 0.27	1.83 ± 0.27	$[\frac{9}{2}^+ - \frac{11}{2}^+]$
	34950 ± 200	700 ± 100	400 ± 200	5.98 ± 0.86	only α_1	$[\frac{9}{2}^+ - \frac{11}{2}^+]$
	41300 ± 200	2000 ± 200		20.19 ± 2.02	11.10 ± 1.50	
	85200 ± 800					
	108500 ± 1100					
Skelton *et al.* [13,29][b]	5800 ± 2000				$\leqslant 6.4$	
	22400 ± 2000				$\leqslant 2.5$	
	42000 ± 2000				14 ± 1.4	
Koehler *et al.*[c]	5793 ± 40		240 ± 200		6.6 ± 1.7	$[\frac{7}{2}^- - \frac{13}{2}^-]$
	35000 ± 500		8200[d] ± 3000			$[\frac{7}{2}^- - \frac{13}{2}^-]$
Doukellis [32]	4700					$\frac{11}{2}^+$
	22300					$\frac{11}{2}^+$
	33230					$\frac{9}{2}^+$

[a]Obtained from the Voigt fits.
[b]Obtained from the inverse ^{23}Na$(\alpha, n)^{26}$Mg reaction.
[c]Uncertainties on the energy position are estimated through the ^{36}Cl(n, p) measurement of Koehler *et al.* [31].
[d]Deduced from the ^{26}Al$(n, p)^{26}$Mg data of Koehler *et al.* [11].

Δ_G, and the Breit-Wigner part represents the natural line width Γ. A Voigt fitting procedure has been performed for the ^{26}Al$(n, \alpha_0 + \alpha_1)^{23}$Na resonances observed in this work. The resulting Voigt fits are shown in Fig. 6. The experimental broadening contribution was calculated and kept fixed during the fit. This experimental broadening is plotted in Fig. 7 together with the total width $\Gamma_V = \sqrt{\Delta_G^2 + \Gamma^2}$ obtained from the Voigt fit at the resonance energies. Only when the total fitted width Γ_V is significantly larger than the calculated broadening width Δ_G can the fitted natural level width Γ be regarded as the real natural line width of that resonance. Figure 7 shows that the natural line width can be determined for only the first two resonances and probably the third resonance.

The parameters obtained from the Voigt fits (energy position, area, and total level width) for each resonance are listed in Table II. The resonance strength ω_α can be calculated from the resonance area using the formula

$$\omega_\alpha = \frac{k_{\text{res}}^2}{2\pi^2} A_{\text{res}}, \tag{2}$$

with $k_{\text{res}}^2[1/b] = 4.826 \times 10^{-6} E_{\text{res}}$ (eV) [28]. The ω_α values given include both the α_0 and α_1 transitions, while the ω_{α_0} values represent the α_0 transitions determined with the help of Fig. 4. The ω_{α_0} values can be compared with the strengths obtained by Skelton *et al.* [29] and Koehler *et al.* [11], reported in Table II. Koehler *et al.* could fit the natural line width for two resonances. Since they measured the ^{26}Al(n, α_0) cross section only up to 10 keV, the parameters of the 35 keV resonance are deduced from their ^{26}Al(n, p) measurement. The results of Skelton *et al.* are obtained from the inverse reactions ^{26}Mg$(p, n)^{26}$Al and ^{23}Na$(\alpha, n)^{26}$Mg [13] via the method of detailed balance [30].

It can be concluded that the uncertainties on the energy position obtained in this work are much smaller than in the previous data thanks to the better energy resolution of the GELINA facility. The resonance strengths obtained in this work are in reasonable agreement with the previous measurements.

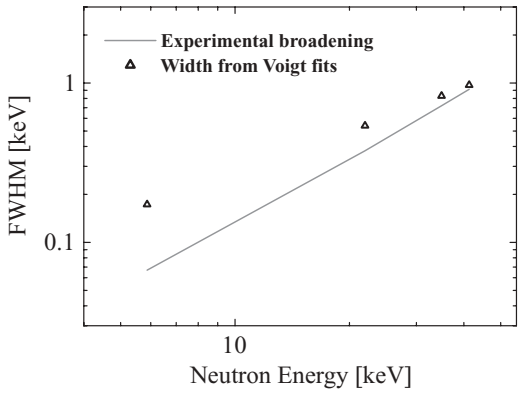

FIG. 7. Total fitted width represented by triangles compared with the calculated experimental broadening (gray line) for the four observed resonances.

2. *Spin assignments*

s-wave ($\ell = 0$) neutrons interacting with the $I^\pi = 5^+$ ground state of ^{26}Al can populate the $J^\pi = \frac{9}{2}^+$ and $J^\pi = \frac{11}{2}^+$ states of the compound nucleus ^{27}Al, whereas *p*-wave ($\ell = 1$) neutrons can populate states from $J^\pi = \frac{7}{2}^-$ through $J^\pi = \frac{13}{2}^-$. The formed states decay to the ground ($J^\pi = \frac{3}{2}^+$) or first excited state ($J^\pi = \frac{5}{2}^+$) of ^{23}Na by emitting α_0 or α_1 particles, respectively. The smallest angular momenta of the emitted

TABLE III. Smallest allowed angular momenta of the emitted α particles from the formed compound nucleus ^{27}Al in the case of impinging s- or p-wave neutrons.

J^π ^{23}Na	J^π ^{27}Al					
	s-wave		p-wave			
	$\frac{9}{2}^+$	$\frac{11}{2}^+$	$\frac{7}{2}^-$	$\frac{9}{2}^-$	$\frac{11}{2}^-$	$\frac{13}{2}^-$
$\frac{3}{2}^+$	4	4	3	3	5	5
$\frac{5}{2}^+$	2	4	1	3	3	5

α particles allowed by the selection rules are tabulated in Table III.

a. Resonance at 5.87 keV. The following formula can be used to calculate the thermal contribution of the three resonances of Table II for which the natural line width Γ could be determined:

$$\sigma(E_{\text{th}}) = \frac{1}{2\pi\sqrt{E_{\text{th}}}} \frac{\Gamma\, A}{E^{3/2}}, \tag{3}$$

with $E_{\text{th}} = 0.0253$ eV, A the area of the resonance in b eV, and Γ and E in eV. If the calculated value is higher than the measured thermal cross section, the resonance can in principle not be s-wave, since only the tails of s-wave resonances contribute to the thermal cross section. With the help of formula (3), a thermal contribution of 941 mb was calculated for the first resonance at 5.87 keV. This resonance is mainly a transition to the ground state of ^{23}Na. This calculated thermal contribution is much higher than the experimentally determined thermal $(n_{\text{th}}, \alpha_0)$ cross section of 261 mb [22]. Therefore, this resonance is classified as a p-wave resonance, with spin J^π from $\frac{7}{2}^-$ through $\frac{13}{2}^-$.

b. Resonance at 22 keV. The second resonance at 22 keV is an α_0 transition and has a calculated thermal cross section contribution of 41 mb, which is lower than the measured $\sigma(n_{\text{th}}, \alpha_0)$ value of 261 mb [22]. So, this resonance can be classified as an s-wave resonance with spin $J^\pi = \frac{9}{2}^+$ or $\frac{11}{2}^+$.

c. Resonance at 35 keV. The third resonance at 35 keV gives a thermal cross section contribution of 44 mb and is an α_1 transition. The experimentally determined thermal $(n_{\text{th}}, \alpha_1)$ cross section is 74 mb [22], so this resonance probably is an s-wave, and the spin of the state is $\frac{9}{2}^+$ or $\frac{11}{2}^+$.

d. Conclusions. In Table II, the spin assignments of this work are compared with those by Koehler *et al.* [11] and by Doukellis [32] which are based on the measurements of Skelton *et al.* [29]. The difference in spin assignment for the third resonance around 35 keV between Koehler and this work can be explained by the great difference in natural line width. Taking the value of Koehler *et al.* [11] to calculate the thermal contribution in the case of an s-wave resonance leads to a thermal contribution which exceeds the measured value of 261 mb.

In principle, interference effects can reduce the contribution to the thermal cross section, leaving open the possibility of a different spin assignment for some resonances. However, this would lead to a non 1/v behavior of the cross section at low energies, which is not the case according to the measurements by Koehler *et al.* [11].

3. Determination of the partial level widths

For the determination of the partial level widths, only two equations are available:

$$\Gamma = \Gamma_\gamma + \Gamma_n + \Gamma_p + \Gamma_\alpha, \tag{4}$$

and

$$A_{\text{res}} = 2\left(\frac{\pi}{k_{\text{res}}}\right)^2 g \frac{\Gamma_n\, \Gamma_\alpha}{\Gamma}, \tag{5}$$

where g represents the statistical factor

$$\frac{2J+1}{(2s+1)(2I+1)}, \tag{6}$$

with J the total angular momentum of the compound nucleus, formed by the target (spin I) and the neutron with spin s and orbital momentum $\ell(\vec{J} = \vec{s} + \vec{l} + \vec{I})$. Even if the often used value for $\Gamma_\gamma = 1$ eV in this mass region is adopted [33], four parameters are left to be fixed: g (through the spin), Γ_n, Γ_p, and Γ_α. With only two equations, it is not possible to solve this system of equations unambiguously. For this reason, no partial level widths could be determined. Additional measurements are necessary, for instance, ^{26}Al(n, γ), ^{26}Al(n, p), or total cross section measurements leading to the same compound nucleus. They will provide more equations so that the partial level widths can be determined. Then they may be used as input parameters in resonance shape analysis (RSA) programs to accurately determine the spin and total and partial level widths of the states in the compound nucleus.

IV. DETERMINATION OF THE MACS

Numerical integration of the obtained $(n, \alpha_0 + \alpha_1)$ cross section data using Eq. [34]

$$\langle\sigma\rangle = \frac{2}{\sqrt{\pi}} \frac{1}{(kT)^2} \int_0^{+\infty} \sigma(E_\mu) E_\mu e^{-\frac{E_\mu}{kT}}\, dE_\mu, \tag{7}$$

with E_μ the center-of-mass neutron energy, leads to the ^{26}Al(n, α) MACS values. They are compared in Fig. 8 with the experimental (n, α_0) values of Koehler *et al.* [11] and Skelton *et al.* [13] and with the theoretical calculations MOST [35], NON-SMOKER [36] and older theoretical values of Caughlan and Fowler [37]. In this work, the (n, α) cross section determination reached an energy $E_f \cong 45$ keV, which means that the integration upper limit of $+\infty$ in the previous formula is replaced by 45 keV, giving rise to systematic uncertainties in the calculated MACS values [34]. If the widths of the resonances are much smaller than the kT value, Eq. (7) may be approximated by the expression [28,34]

$$\langle\sigma\rangle = \sigma_{\text{th}} \sqrt{\frac{0.0253}{kT}} + \frac{2}{\sqrt{\pi}} \frac{1}{(kT)^2} \sum_{\text{res}} A_{\text{res}} E_{\text{res}} e^{-\frac{E_{\text{res}}}{kT}}. \tag{8}$$

Taking the derivative of this equation with respect to kT, one can show that a resonance at an energy E_{res} has its maximum contribution to the MACS at $kT = E_{\text{res}}/2$. This means that

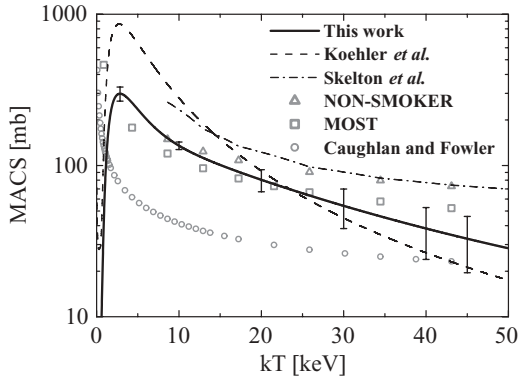

FIG. 8. ^{26}Al$(n, \alpha_0 + \alpha_1)^{23}$Na MACS values calculated by numerical integration of the obtained cross section data (black line). A comparison is made with the experimental values from Koehler *et al*. [11] and Skelton *et al*. [13] and with theoretical values. The latter ones are represented by gray symbols.

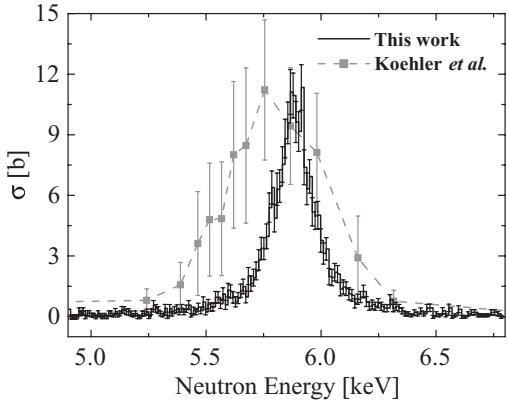

FIG. 9. Cross section data obtained for the first resonance at 5.9 keV (black line) compared with the data of Koehler *et al*. [11] (gray dashed line). The resonance area obtained by Koehler is much higher (but less precise) than the area obtained in this work, as indicated by the ω_{α_0} value in Table II.

if the cross section is known up to an energy E_f, MACS values above $E_f/2$ are mainly originating from resonances at energies higher than E_f. Therefore, the calculated MACS values should be regarded as lower limits above $E_f/2$. So the obtained MACS values have to be considered as lower limits for kT above 22 keV. The obtained MACS values in the energy region $kT \leqslant 22$ keV are much lower than the values obtained by Koehler *et al*. [11]. However, they are in reasonable agreement with the newest theoretical values. It is easily explained why the MACS values of Koehler *et al*. [11] around 3 keV are much higher than the ones obtained here: the resonance area or strength for the resonance at 5.87 keV in the experiment of Koehler *et al*. [11] is much higher, as shown in Fig. 9 and listed in Table II. When comparing, one should, however, take into account the 26% uncertainty on the data of Koehler *et al*. [11]. Because the experiment of Koehler *et al*. [11] reached approximately 10 keV, their MACS values are lower limits for kT above 5 keV.

The present results were used in stellar AGB models by Gallino *et al*. [38], and they concluded that ^{26}Al is severely depleted by neutron captures in AGB stars.

V. CONCLUSIONS

The ^{26}Al$(n, \alpha_0)^{23}$Na + ^{26}Al$(n, \alpha_1)^{23}$Na reaction cross section has been measured up to about 100 keV. Four resonances were analyzed and two others were identified at higher energies. For the first four, a resonance analysis determined the resonance area, total level width, and spin of the relevant states in ^{27}Al, where a higher precision compared to previous experiments was obtained thanks to the much better energy resolution of the GELINA facility.

The calculated MACS values were used in stellar AGB models by Gallino *et al*. [38], resulting in a severe depletion of ^{26}Al by neutron captures in AGB stars.

[1] W. A. Mahoney, J. C. Ling, W. A. Wheaton, and A. S. Jacobson, Astrophys. J. **286**, 578 (1984).
[2] U. Oberlack, Ph.D. thesis, Technische Universität München, 1997.
[3] G. J. Wasserburg, M. Busso, R. Gallino, and K. M. Nollett, Nucl. Phys. **A777**, 5 (2006).
[4] N. Mowlavi, AIP Conf. Proc. **425**, 507 (1998).
[5] J. C. Lattanzio and C. A. Frost, in *Fundamental Stellar Properties: The Interaction between Observation and Theory* (Springer, New York, 1997).
[6] J. C. Lattanzio, New Astron. Rev. **46**, 469 (2002).
[7] O. Straniero, R. Gallino, and S. Cristallo, Nucl. Phys. **A777**, 311 (2006).
[8] G. Meynet and M. Arnould, in *Origin and Evolution of the Elements* (Cambridge University, Cambridge, England, 1993), p. 539.
[9] A. I. Karakas and J. C. Lattanzio, in *Origin and Evolution of the Elements,* Carnegie Observatories Astrophysics Series Vol. 4 (Cambridge University, Cambridge, England, 2004).
[10] C. E. Rolfs and W. S. Rodney, *Cauldrons in the Cosmos* (University of Chicago, Chicago, 1988).
[11] P. E. Koehler, R. W. Kavanagh, R. B. Vogelaar, Y. M. Gledenov, and Y. P. Popov, Phys. Rev. C **56**, 1138 (1997).
[12] H. P. Trautvetter, H. W. Becker, U. Heinemann, L. Buchmann, C. Rolfs, F. Käppeler, M. Baumann, H. Freiesleben, H. J. Lütke-Stetzkamp, P. Geltenbort *et al*., Z. Phys. A **323**, 1 (1986).

[13] R. T. Skelton, R. W. Kavanagh, and D. G. Sargood, Phys. Rev. C **35**, 45 (1987).
[14] J. Wagemans, Ph.D. thesis, Universiteit Gent (Belgium), 2000.
[15] L. De Smet, C. Wagemans, G. Goeminne, J. Wagemans, J. Heyse, and J. Van Gils, Nucl. Phys. **A758**, 80c (2005).
[16] L. De Smet, Ph.D. thesis, Universiteit Gent (Belgium), 2006, https://archive.ugent.be/1854/5849.
[17] W. Mondelaers and P. Schillebeeckx, Notiziario Neutroni e Luce di Sincrotrone **11.2**, 19 (July 2006).
[18] A. Bensussan and J. M. Salome, Nucl. Instrum. Methods **155**, 11 (1978).
[19] J. Gonzales, C. Bastian, S. de Jonge, and K. Hofmans, Modular Multiparameter Multiplexer MMPM, Hardware Description and User Guide, 1997, IRMM Geel (Belgium) Internal Report GE/R/INF/06/97 (unpublished).
[20] C. Ingelbrecht, A. Moens, R. Eykens, and A. Dean, Nucl. Instrum. Methods Phys. Res. A **397**, 34 (1997).
[21] C. Ingelbrecht, J. Ambeck-Madsen, K. Teipel, P. Robouch, G. Arana, and S. Pomme, Nucl. Instrum. Methods Phys. Res. A **438**, 36 (1999).
[22] J. Wagemans, C. Wagemans, G. Goeminne, P. Geltenbort, and A. Moens, Nucl. Phys. **A696**, 31 (2001).
[23] C. Ingelbrecht, A. Moens, J. Wagemans, B. Denecke, T. Altzitzoglou, and P. Johnston, Nucl. Instrum. Methods Phys. Res. A **480**, 114 (2002).
[24] L. De Smet, C. Wagemans, G. Goeminne, J. Heyse, and J. Van Gils, Phys. Rev. C **75**, 034617 (2007).
[25] http://t2.lanl.gov/cgi-bin/nuclides/endind.
[26] C. Bastian, in *Proceedings of the International Conference on Neutron Research and Industry, 1996*, Crete, Greece, The Int. Society for Optical Engineering, Vol. 2867, 611 (1997).
[27] C. Bastian, A. Borella, F. Gunsing, J. Heyse, S. Kopecky, G. Noguere, P. Siegler, and P. Schillebeeckx, in *PHYSOR-2006* (American Nuclear Society, LaGrange Park, IL, 2006).
[28] R. L. Macklin and J. H. Gibbons, Rev. Mod. Phys. **37**, 166 (1965).
[29] R. Kavanagh (private communication).
[30] W. A. Fowler, G. R. Cauglan, and B. A. Zimmerman, Annu. Rev. Astron. Astrophys. **5**, 525 (1967).
[31] P. E. Koehler, S. M. Graff, H. A. O'Brien, Y. M. Gledenov, and Y. P. Popov, Phys. Rev. C **47**, 2107 (1993).
[32] G. Doukellis, Nuovo Cimento **A101**, 651 (1989).
[33] S. F. Mughabghab, *Atlas of Neutron Resonances* (Elsevier, Amsterdam, 2006), 5th ed.
[34] H. Beer, F. Voss, and R. R. Winters, Astrophys. J. Suppl. Ser. **80**, 403 (1992).
[35] S. Goriely, http://www-astro.ulb.ac.be/Html/ncap.html.
[36] T. Rauscher, http://nucastro.org/reaclib.html.
[37] G. R. Caughlan and W. A. Fowler, At. Data Nucl. Data Tables **40**, 283 (1988).
[38] R. Gallino (private communication).